Radiographic Testing of Anomalies in Thick Metal Components: Fitting the Standard Line-Integral Model

Marc C. Robini, *Member, IEEE*, and Isabelle E. Magnin, *Member, IEEE*

***Abstract*—Radiography is an effective method for nondestructive inspection of thick metal components. However, complete diagnosis of internal defects is a difficult task that needs reliable computer assistance. In particular, fully 3-D reconstruction would be a very valuable tool for the expert, but it is not so clear whether digitized radiographs can be made suitable for reconstruction. We show that this is indeed the case by studying the radiographic image formation process in the context of primary loop piping inspection in pressurized water nuclear reactors. In a more general way, our findings apply to the testing of thick metal pecimens with simple, known geometry. Based on justified simplifications and approximations, we demonstrate that it is possible to process the raw data to closely fit the conventional line-integral projection model. More specifically, we provide a full processing procedure that includes (i) a criterion for subsampling the data without loss of pertinent information, (ii) a novel field-flattening algorithm, and (iii) a calibration method that requires minimal knowledge about the data acquisition parameters. The actual 3-D reconstruction issue is addressed in another paper [1] whose results further validate the present work.**

***Index Terms*—Data models, field-flattening, image processing, nondestructive testing, nuclear imaging, radiography, scattering.**

I. Introduction

A. Motivation and Contribution

OUR study is motivated by a nondestructive evaluation task that plays a vital role in the nuclear power plant maintenance program of the EDF group, namely the radiographic inspection of flaws in casted elbows of the primary loop of pressurized water reactors [2]. These components undergo regular checks, as they are subject to severe temperature and pressure conditions that may lead to structural flaw formation or worsen existing anomalies. The testing procedure consists in introducing a gamma-ray source inside the inspected pipe and recording the outgoing radiation by means of X-ray films flattened against the external surface. Because of the large specimen thickness (about 7–8 cm), the angle of incidence is limited and only five to seven radiographs are generally available for a given defect. Consequently, building up a complete diagnosis including precise localization, orientation, and shape characterization of flaws is a difficult task that needs reliable computer assistance. The issue at stake here is to demonstrate the feasibility of reconstructing the 3-D shape of voids (such as gas holes, airlocks, shrinkage cavities, or cracks) by considering real test data gathered under conditions similar to those met on site. This turns out to be a great challenge since dealing with a few 2-D projections collected under a limited angle of incidence is not the only difficulty: first, due to scattered radiation predominance, and because the flaw size is small with respect to the specimen thickness, both the signal-to-noise ratio (SNR) and the contrast are low; second, the scattered radiation and, in our case, the digitization apparatus produce unknown, smooth gradients of luminosity which contaminate the attenuation data; third, the projections are not calibrated in the sense that the flaw information signals are weighted by unknown constants.

Let $\{d^k; k = 1, \dots, K\}$, $d^k = \{d^k_s; s \in G^k\}$, be a set of 2-D digitized projections available for reconstruction, where G^k denotes a rectangular pixel lattice. Many authors (see, e.g., [3]–[6] for closely related problems) resort to the standard direct model

$$d^k = \mathcal{H}^{(k)}(x^0) + \eta^k \tag{1}$$

where the field $x^0 = \{x^0_v; v \in V\}$, defined over a 3-D voxel lattice V, characterizes the shape of the defects, $\mathcal{H}^{(k)}$ is a linear map from $\mathbb{R}^{|V|}$ to $\mathbb{R}^{|G^k|}$, and η^k is Gaussian white noise with mean zero and variance σ_k^2 (which we denote by $\eta^k \sim \mathcal{N}(0, \sigma_k^2)$ whether σ_k is a constant field or not). However, to our knowledge, no attempt was made to rigorously justify this model for the testing of thick metal components in the context of a real industrial application. This task constitutes the main focus of this paper; the actual 3-D reconstruction issue is discussed in [1]. Assuming that the inspected object geometry is known, we show that, at the expense of some model-driven processing of the data, one can indeed come up with a set of projections of the form

$$d^k \approx \omega \Upsilon^k + \eta^k \tag{2}$$

for some constant ω close to one and independent of k, where the field Υ^k is directly connected to the attenuation of a monochromatic radiation by the "negative" of the flaws (i.e., by metal objects taking the shape of the defects). These projections fit well into model (1) for small size flaws such as those we wish to characterize.

Manuscript received July 12, 2006; revised April 27, 2007. This work was supported by Électricité de France who also supplied the data and associated human expert know-how. This material was presented in part at the IEEE Nuclear Science Symposium, San Diego, CA, November 2007. This work has been performed in accordance with the scientific trends of the national research group GDR ISIS of the CNRS.

The authors are with CREATIS (CNRS Research Unit UMR5520 and INSERM Research Unit U630), INSA Lyon, 69621 Villeurbanne cedex, France (e-mail: marc.robini@insa-lyon.fr).

Digital Object Identifier 10.1109/TNS.2007.901219

B. Overview

In Section II, we provide a brief description of the experimental setup — the real data presented therein will be used throughout the rest of the paper. Section III is devoted to the analysis of the image formation process, except for scattered radiation which is studied in Section IV. We show that the film exposure E satisfies

$$E \approx \tau\widetilde{\mathcal{I}}_{\rm pri}(1+\mathcal{I}_{\rm scat}/\widetilde{\mathcal{I}}_{\rm pri}+\Upsilon) \tag{3}$$

where τ is the exposure time, $\mathcal{I}_{\rm scat}$ denotes the irradiance produced by scattered photons, $\widetilde{\mathcal{I}}_{\rm pri}$ stands for the primary irradiance that would be observed in the absence of defect, and Υ is the flaw information signal. In addition, we establish that the common logarithm of the available digital radiographs, say $\log_{10} P$, is related to E through an expression of the form

$$\log_{10} P \approx \mathfrak{I}_0 - \omega_1 E + \eta_1, \qquad \eta_1 \sim \mathcal{N}(0,\omega_2 E)$$

where $\mathfrak{I}_0$ is an unknown, smoothly varying field resulting from digitization and ω_1, ω_2 are unknown positive constants. The primary irradiance $\widetilde{\mathcal{I}}_{\rm pri}$ in (3) can be easily estimated, but the scattered component $\mathcal{I}_{\rm scat}$ is a real nuisance for extracting Υ. However, it is intuitively reasonable to assume that $\mathcal{I}_{\rm scat}$ is not sensitive to moderate size flaws. Indeed, starting with a single-scatter approximation, it is shown in Section IV that the term $1 + \mathcal{I}_{\rm scat}/\widetilde{\mathcal{I}}_{\rm pri} =: \widetilde{B}$ can be approximated by the spatial distribution of the build-up factor that would be observed if the inspected object were flawless.

Section V discusses how to obtain projection data of type (2) from our model:

$$\log_{10} P \approx \mathfrak{I}_0 - \omega_1\tau\widetilde{\mathcal{I}}_{\rm pri}(\widetilde{B}+\Upsilon) + \eta_1.$$

In the prospect of reducing computational costs, we first demonstrate that the digitized radiographs can be subsampled without loss of useful flaw information. Strictly speaking, we give an upper bound on the subsampling factor that permits one to retain the flaw information located in the frequency regions where the Fourier domain SNR is greater than one. Next, we propose a novel field-flattening algorithm to remove the unknown, smooth component $\mathfrak{I}_0 - \omega_1\tau\widetilde{\mathcal{I}}_{\rm pri}\widetilde{B} =: F_0$. This is a quite difficult task, as the support of Υ is not known *a priori* and as the spectral ranges of Υ and F_0 significantly overlap. Our algorithm performs well even for very low SNR data; it leads to projections of the form $\omega_1^k\Upsilon^k + \eta_2^k$ for some set of constants $\{\omega_1^k; k = 1,\ldots,K\}$, where η_2^k is a nonstationary, zero-mean, Gaussian white noise field. The last stage is to get rid of the ω_1^k's up to a multiplicative constant ω preferably close to one. For this purpose, we develop a calibration procedure that does not depend on film characteristics, exposure time, or source activity. This ultimately leads to projections of type (2), as confirmed by comparing simulations to experimental results. The full processing procedure is summarized in Section VI, where we also give concluding remarks about how to obtain model (1) from (2).

II. Experimental Setup

Gamma-ray data have been collected under the constraints imposed by on-site testing conditions. The inspected specimens

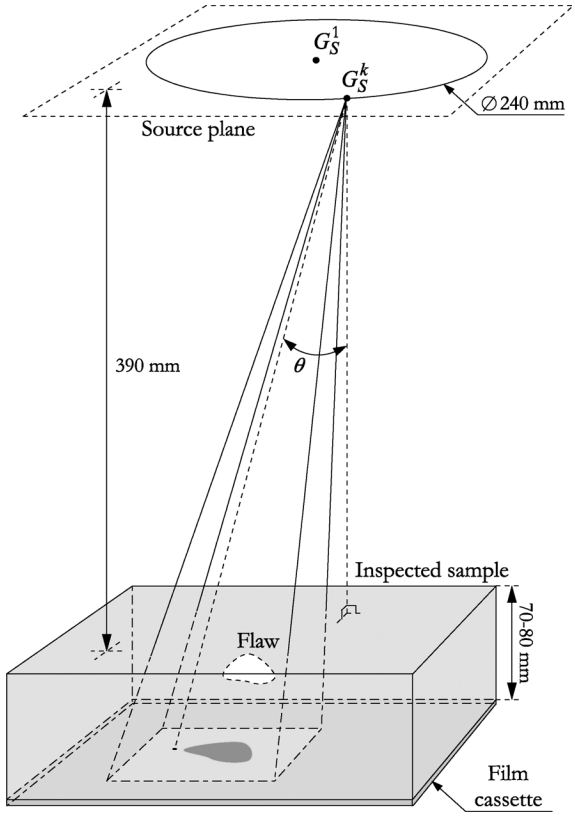

Fig. 1. Data acquisition geometry.

are nitrogen-strengthened austenitic stainless steel castings with uniform thickness of 7 or 8 cm including artificial flaws with known shape, dimensions, and localization. In accordance with Fig. 1, the source positions $G_S^1 \ldots, G_S^K$ are in a plane parallel to the base of the specimen. The film cassettes are taped on the specimen and the source-film distance is fixed by the external diameter of the pipes to be inspected. Within the source plane, $G_S^2, \ldots, G_S^K$ lie on a circle whose center G_S^1 and whose diameter are chosen to ensure an upper thickness limit of 110% of the specimen thickness in the projection regions of interest. Therefore, the angle of incidence θ is less than 25 degrees. Each film cassette contains a 2 mm lead filter and is backed with a 3 mm lead screen for protection against backscatter. In addition, the films are sandwiched between 0.2 mm lead intensifying screens whose main effect is to convert part of the ionizing radiation into electrons that assist in the formation of the latent image. The sources are 3 mm $\times$ 3 mm iridium-192 cylindrical pellets with strength close to 100 Ci and the exposure times varies between 2 and 5 hours as a function of source position and specimen thickness. Note that on-site inspections are scheduled during shutdown periods that are long enough to assume constant temperature and pressure conditions.

After film development, digitization is achieved by placing films on an illuminated screen and recording the transmitted irradiance using a CCD array camera. This system allows one to obtain 5 cm square projections with spatial resolution $\Delta = 50\ \mu$m, some examples of which are given in Fig. 2. The radiographs in Figs. 2(a)–(d) show an open notch, fabricated by electro-erosion, simulating a crack with a large depth/width

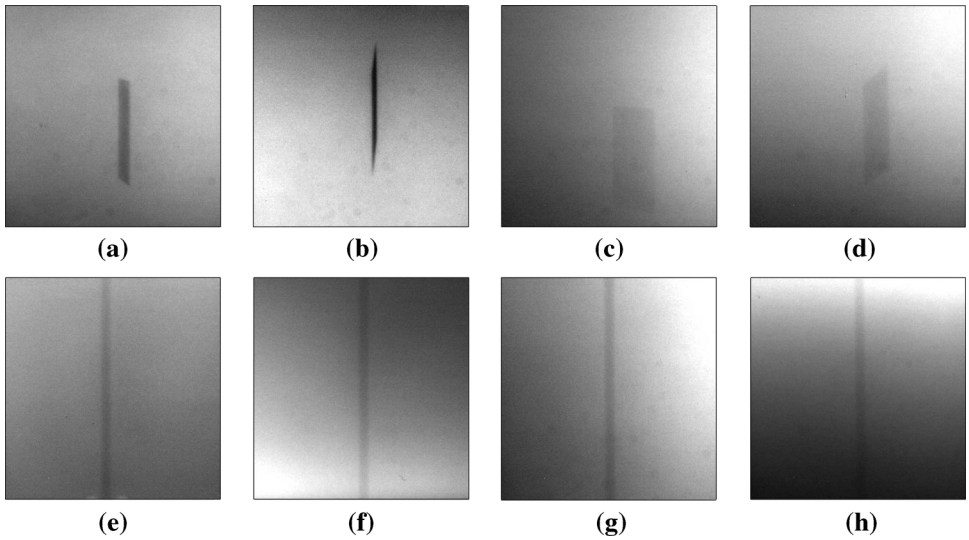

Fig. 2. Digital radiograph examples: (a)–(d) 20×20 mm $\times$ 0.3 mm electro-eroded notch; (e)–(h) 2 mm diameter drilled hole.

ratio. Figs. 2(e)–(h) are views of a 2 mm diameter hole parallel to the base of the specimen at a depth of 10 mm on the source side. Note that the smooth background intensity variations are not representative of metal thickness, as the incident irradiance produced by the illuminator of the digitization apparatus is not constant. This could be avoided by using a laser digitizer, but there was not one available at the time of the experiments (the data acquisition process was outside our control).

III. Image Formation Model

The data model we develop here is dedicated to the experimental setup described in Section II, but it can be easily customized to other radiographic inspection systems for thick metal components. The results presented in Sections III-A and III-B are to be interpreted as statistical averages; deviations from this mean behavior is the subject of Section III-C.

A. The Radiant Image

When the detector is an X-ray film, the information to be captured is the energy fluence that exposed the emulsion. This quantity, called exposure and denoted by E, is obtained by integrating the irradiance (i.e., the energy fluence rate) over the exposure period. For iridium-192 sources, the radioactive decay over a several hours period is negligible and the relevant forms of interactions of photons with matter are photoelectric absorption and scattering. Hence, for any point r in the detector plane

$$E(r) \approx \tau \left(\mathcal{I}_{\mathrm{pri}}(r) + \mathcal{I}_{\mathrm{scat}}(r) \right) \tag{4}$$

where τ is the exposure time and $\mathcal{I}_{\mathrm{pri}}$ and $\mathcal{I}_{\mathrm{scat}}$ denote the energy fluence rates respectively produced by primary (i.e., unscattered) and scattered photons. The remainder of this subsection is devoted to the characterization of the primary component (scattered radiation is studied in Section IV).

Consider the geometry shown in Fig. 3. For any point s in the source S, $Q(s)$ is the distance from s to the detector plane Π_{d} and, given any point $r \in \Pi_{\mathrm{d}}$, $R(s,r)$ denotes the distance from s to r. Let $\mu(a,\nu)$ be the total linear attenuation coefficient at point a for energy $h\nu$ (h is Planck's constant) and let

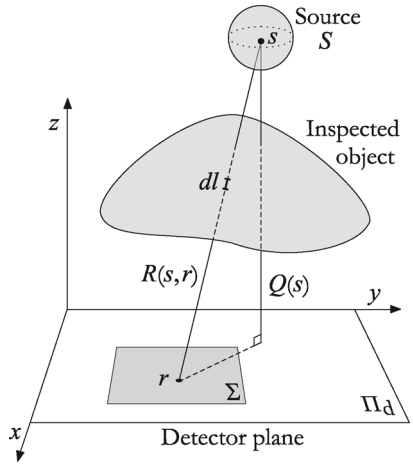

Fig. 3. Geometry used for modeling the primary irradiance.

$\int_s^r \mu(l,\nu)dl$ be the line integral running from s to r. The primary irradiance can be written as

$$\mathcal{I}_{\mathrm{pri}}(r) = \frac{\mathcal{A}}{4\pi\mathcal{V}} \times \sum_j \left\{ \alpha_j h\nu_j \int_S \exp\left(-\int_s^r \mu(l,\nu_j)dl \right) \frac{Q(s)}{R^3(s,r)} d^3s \right\},$$

where $\mathcal{V}$ is the volume of the source, $\mathcal{A}$ is the source activity, and α_j denotes the probability that a disintegration is accompanied by the emission of a photon of energy $h\nu_j$. Our experimental conditions allows us to make useful simplifications.

- First, letting μ_0 (respectively, μ_{filt}) be the total linear attenuation coefficient of the material composing the inspected object (respectively, the filter), we have

$$\int_s^r \mu(l,\nu)dl = \mu_0(\nu)\left(\widetilde{L}(s,r) - L_{\mathrm{flaw}}(s,r) \right) + \mu_{\mathrm{filt}}(\nu) L_{\mathrm{filt}}(s,r)$$

where $\widetilde{L}(s,r)$, $L_{\rm flaw}(s,r)$ and $L_{\rm filt}(s,r)$ respectively denote the lengths of intersection between line segment $[sr]$ and the flawless specimen, the flaw(s) and the filter. In our case, $\mu_0 \approx \mu_{\rm Fe}$ and $\mu_{\rm filt} = \mu_{\rm Pb}$, where $\mu_{\rm Fe}$ and $\mu_{\rm Pb}$ are the total linear attenuation coefficients of iron and lead.

- Second, because the source dimensions are very small compared to the source-film distance, we can set $Q(s) \approx Q(G_S) =: \mathcal{Q}$ and $R(s,r) \approx R(G_S,r) =: \mathcal{R}(r)$ over the projection region of interest Σ. To the same order of approximation, since the inspected specimen and the filter have uniform thickness, $\widetilde{L}(s,r) \approx \widetilde{L}(G_S,r) =: \widetilde{\mathcal{L}}(r)$ and $L_{\rm filt}(s,r) \approx L_{\rm filt}(G_S,r) =: \mathcal{L}_{\rm filt}(r)$.

Taking this into account, we obtain

$$\mathcal{I}_{\rm pri}(r) \approx \frac{\mathcal{A}\mathcal{Q}}{4\pi\mathcal{V}\mathcal{R}^3(r)} \int\limits_S \sum_j \mathcal{Z}_j(s,r) d^3s \tag{5}$$

with

$$\mathcal{Z}_j(s,r) := \alpha_j h\nu_j \exp\Big\{ -\mu_0(\nu_j)\Big(\widetilde{\mathcal{L}}(r) - L_{\rm flaw}(s,r)\Big) - \mu_{\rm filt}(\nu_j)\mathcal{L}_{\rm filt}(r)\Big\}.$$

The limited angle of incidence opens the way to another simplification: for any possible source position, we can find α_0 and $h\nu_0$ such that

$$\forall (s,r) \in S \times \Sigma, \quad \sum_j \mathcal{Z}_j(s,r) \approx \mathcal{Z}_0(s,r). \tag{6}$$

In other words, from the primary irradiance standpoint, the real source behaves like a monochromatic source with activity $\alpha_0\mathcal{A}$ and frequency ν_0. Finding α_0 and $h\nu_0$ is an easy to solve nonlinear optimization task which can be performed regardless of the shape of the defects [2]. For instance, Fig. 4 displays the results associated with the testing conditions described in Section II in the least favorable situation (i.e., when the mean angle of incidence over Σ is 25 degrees). The estimated quantities and the corresponding relative error

$$\varepsilon_0 := \frac{\sup\limits_{(s,r)\in S\times\Sigma} \Big| \mathcal{Z}_0(s,r) - \sum_j \mathcal{Z}_j(s,r) \Big|}{\sum_j \mathcal{Z}_j(s,r)}$$

are plotted versus $L^\star_{\rm flaw} := \sup_{(s,r)\in S\times\Sigma} L_{\rm flaw}(s,r)$. For small defects (e.g., $L^\star_{\rm flaw} \leqslant 1$ cm), ε_0 is of the order of 10^{-3} and the numeric values of α_0 and $h\nu_0$ stay close to those obtained for a flawless specimen (i.e., for $L^\star_{\rm flaw} = 0$). This shows that the proposed approximation is sharp and that the specification of the equivalent sources can be accomplished on the sole basis of the specimen geometry.

From (4), (5) and (6), the exposure can be described by

$$E(r) \approx \tau\widetilde{\mathcal{I}}_{\rm pri}(r)\Big(1 + \mathcal{I}_{\rm scat}(r)/\widetilde{\mathcal{I}}_{\rm pri}(r) + \Upsilon(r)\Big) \tag{7}$$

where

$$\Upsilon(r) := \mathcal{V}^{-1} \int\limits_S \left(\exp\left(\mu_0(\nu_0) L_{\rm flaw}(s,r)\right) - 1\right) d^3s$$

$$\approx \mu_0(\nu_0)\mathcal{V}^{-1} \int\limits_S L_{\rm flaw}(s,r) d^3s \tag{8}$$

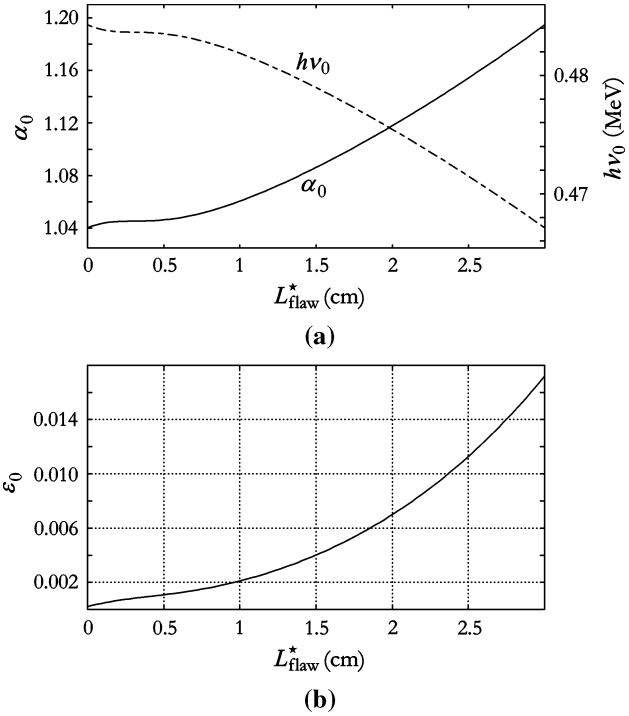

Fig. 4. (a) Equivalent monochromatic source characteristics and (b) associated relative error versus maximum path length through defect cavities.

conveys the pertinent flaw information, and where $\widetilde{\mathcal{I}}_{\rm pri}$ denotes the primary irradiance that would be "observed" in the absence of defect:

$$\widetilde{\mathcal{I}}_{\rm pri}(r) \approx \alpha_0 \mathcal{A} h\nu_0 \widetilde{\Theta}_0(r)$$

where

$$\widetilde{\Theta}_0(r) := \big(\mathcal{Q}/4\pi\mathcal{R}^3(r)\big) \times \exp\Big(-\mu_0(\nu_0)\widetilde{\mathcal{L}}(r) - \mu_{\rm filt}(\nu_0)\mathcal{L}_{\rm filt}(r)\Big) \tag{9}$$

($\widetilde{\Theta}_0(r) d^2r$ is the ratio of the mean number of primary photons intercepted by the detector element d^2r to the number of photons emitted by the equivalent monochromatic source.)

B. Detection and Digitization

The optical density, D, of a developed X-ray film depends linearly on exposure up to $D = 3-4$ (see, e.g., [7]–[9]). The exposure time is typically determined so that this relationship holds within the projection region of interest. Thus,

$$D(r) \approx D_{\rm min} + \Gamma E(r) \tag{10}$$

where the constant Γ measures film sensitivity and where $D_{\rm min} \approx 0.2-0.3$ denotes the fog density resulting from the inherent density of the base of the film together with the presence of self-developable grains in the emulsion. In fact, because of the blurring due to the scattering of electrons in the emulsion, it would be more accurate to write

$$D(r) \approx D_{\rm min} + \Gamma (E * h_{\rm u})(r)$$

where $*$ stands for the 2-D convolution operator and h_{u} is a low-pass filter impulse response. However, this blurring effect is negligible compared to the geometric blurring due to finite source size (the former is of the order of 0.1 mm and the latter is of the order of 1 mm).

As regards digitization, the CCD camera imperfections can be safely overlooked, but the intensity variations produced by the illuminator have to be taken into account. Hence, the available numerical data consist of projections $P = \{P(m,n); 0 \leqslant m,n \leqslant N-1\}$ of the form

$$P(m,n) \approx I_0(m,n) \cdot 10^{-D(m,n)} \tag{11}$$

where I_0 is an unknown, smoothly varying field, and $D(m,n)$ denotes the density measured over the square domain

$$A_{m,n} := [m\Delta,(m+1)\Delta] \times [n\Delta,(n+1)\Delta] \tag{12}$$

whose size Δ is the spatial resolution of the digitization system.

C. Noise Characteristics

Let $\dot{\Phi}(r)$ be the mean number of photons per unit area and unit time (i.e., the fluence rate) impinging on the detector. During the exposure period, photon detection can be described by the spatial random process

$$\mathfrak{n}_{\mathrm{d}}(r) = \sum_{i=1}^{\mathfrak{N}_{\mathrm{d}}} \delta(r - r_i)$$

where δ is the Dirac delta function, $\mathfrak{N}_{\mathrm{d}}$ is the total number of detected photons, and the 2-D vectors r_i are independent and identically distributed random variables with probability density function $\dot{\Phi}(r)/\int_{\Pi_{\mathrm{d}}} \dot{\Phi}(r')d^2r'$. Restricting ourselves to the monochromatic case, the derivation of a noise model for our radiographic images starts with the characterization of the nonstationary discrete random field

$$\left\{ \mathfrak{n}_{\mathrm{d}}(m,n) := \int_{A_{m,n}} \mathfrak{n}_{\mathrm{d}}(r)d^2r; \quad m,n \in \mathbb{Z} \right\} \tag{13}$$

where $A_{m,n}$ is given in (12). Let $\mathcal{E}$ be the quantum efficiency of the detector (i.e., the probability that an incident photon contributes to latent image formation) and let $\mathfrak{N}_{\mathrm{i}}$ be the total number of photons incident on the emulsion. Clearly, $\mathfrak{N}_{\mathrm{d}}$ is a binomial random variable with parameters $\mathfrak{N}_{\mathrm{i}}$ and $\mathcal{E}$. Since $\mathfrak{N}_{\mathrm{i}}$ can be assimilated to a poisson random variable with mean $\tau \int_{\Pi_{\mathrm{d}}} \dot{\Phi}(r)d^2r =: \overline{\mathfrak{N}}_{\mathrm{i}}$, which we denote by $\mathfrak{N}_{\mathrm{i}} \sim \mathcal{P}(\overline{\mathfrak{N}}_{\mathrm{i}})$, we deduce that $\mathfrak{N}_{\mathrm{d}} \sim \mathcal{P}\mathcal{E}\overline{\mathfrak{N}}_{\mathrm{i}})$. It follows that

$$\mathfrak{n}_{\mathrm{d}}(m,n) \sim \mathcal{P}\left(\overline{\mathfrak{n}}_{\mathrm{d}}(m,n)\right)$$

with

$$\begin{aligned} \overline{\mathfrak{n}}_{\mathrm{d}}(m,n) &= \mathcal{E}\tau \int_{A_{m,n}} \dot{\Phi}(r)d^2r \\ &\propto \Delta^{-2} \int_{A_{m,n}} E(r)d^2r =: E[m,n]. \end{aligned}$$

In addition, it is not difficult to check that (13) is uncorrelated:

$$\mathbb{E}\left[\mathfrak{n}_{\mathrm{d}}(m,n)n_{\mathrm{d}}(k,l)\right] - \overline{\mathfrak{n}}_{\mathrm{d}}(m,n)\overline{n}_{\mathrm{d}}(k,l) = \delta_{mn}\delta_{kl}\overline{\mathfrak{n}}_{\mathrm{d}}(m,n)$$

where δ_{ij} is the Kronecker delta symbol.

The above description can be further simplified when using very fine grain films. For an average density of about 2–3 and a 50 μm spatial resolution, the number $\mathfrak{n}_{\mathrm{g}}(m,n)$ of developed grains in the volume of emulsion under $A_{m,n}$ is of the order of 10^3 (which is the reason why granularity is not considered here). Also, for the principal energy spectrum lines of iridium-192 (i.e., between 0.3 MeV and 0.6 MeV) the average number of halide grains that are made developable for each quantum absorbed ranges between 20 and 40. Therefore, $\overline{\mathfrak{n}}_{\mathrm{d}}(m,n)$ is large enough to fully justify a Gaussian approximation

$$\mathfrak{n}_{\mathrm{d}}(m,n) \approx \overline{\mathfrak{n}}_{\mathrm{d}}(m,n) + \left(\overline{\mathfrak{n}}_{\mathrm{d}}(m,n)\right)^{1/2} \eta(m,n)$$

where $\eta \sim \mathcal{N}(0,1)$. Since $\mathfrak{n}_{\mathrm{g}}(m,n)$ is a linear function of $\mathfrak{n}_{\mathrm{d}}(m,n)$ in the range of linearity of the density-exposure relation, the same kind of approximation holds for $\mathfrak{n}_{\mathrm{g}}(m,n)$, but with η correlated. Indeed, two-dimensionally, the set of grains that are rendered developable for one quantum absorbed is confined to a small disc whose diameter, of the order of 0.1 mm, is greater than the spatial resolution. Because $D(m,n)$ is a linear function of $\mathfrak{n}_{\mathrm{g}}(m,n)$ with mean behavior described by (10), we deduce that

$$D(m,n) \approx D_{\min} + \Gamma E[m,n] + \gamma \left(E[m,n]\right)^{1/2} \eta(m,n) \tag{14}$$

for some positive constant γ. It should be stressed that the magnitude of geometric blurring is large, as on-site testing conditions impose small source-film distances. Consequently, the cut-off frequency of the power spectrum of density fluctuations is greater than the useful bandwidth of the mean density distribution $D_{\min} + \Gamma E$. Hence we can actually assume that $\eta \sim \mathcal{N}(0,1)$ in (14).

IV. Scattered Radiation

As suggested by (7), scattered radiation does not contribute to valuable flaw information, but rather reduces the contrast of the radiographs. Moreover, scattering is the dominant interaction in steel and other metallic materials for photons in the iridium-192 spectrum. For large specimen thickness, most photons undergo several scattering events before reaching the detector or being destroyed by photoelectric absorption. In this section, we show that, in comparison with the primary component, the flaw information content in the scattered component is so poor as to be disregarded. In a first analysis, we assume that each detected photon experiences at most one scattering event; this suggests a useful approximation that is validated by Monte Carlo simulation.

Let us focus on the simple transmission imaging geometry shown in Fig. 5, where r and r' are vectors in the detector plane Π_{d} with equation $z = 0$. Without loss of generality, we assume that the scattering medium is between the planes $z = 0$ and $z = z^\star > 0$. Consider a thin pencil of rays of frequency ν and cross-sectional area d^2r', and let $\alpha_\nu([ab])$ be the global attenuation factor along line segment $[ab]$, that is, $\alpha_\nu([ab]) := \int_a^b \mu(l,\nu)dl$.

A volume element $dV = d^2r'dz$ situated along the pencil at a distance z from $\Pi_{\rm d}$ receives the primary fluence rate

$$\dot{\Phi}_{\rm pri}(r',z) := \dot{\Phi}_0(r')\alpha_\nu\left([(r',z^\star)(r',z)]\right)$$

where $\dot{\Phi}_0$ is the incident fluence rate, and the fluence rate per unit solid angle scattered by dV is

$$\dot{\Phi}_{\rm pri}(r',z)\mathfrak{n}_{\rm a}(r',z)\left(\frac{d\sigma^{\rm R}(\theta)}{d\Omega}+\frac{d\sigma^{\rm C}(\theta)}{d\Omega}\right)d^2r'dz \qquad (15)$$

where $\mathfrak{n}_{\rm a}$ is the spatial distribution of atom density and where $d\sigma^{\rm R}(\theta)/d\Omega$ and $d\sigma^{\rm C}(\theta)/d\Omega$ are respectively the differential Rayleigh and Compton scattering cross sections per atom [10] (both quantities depend on ν and (r',z)). The number of photons scattered in the direction of a detector element of area d^2r located at $(r,0)$ is obtained by multiplying (15) with the differential solid angle $d\Omega = zd^2r/R^3$, where

$$R := \left(\|r-r'\|_2^2+z^2\right)^{1/2}.$$

Moreover, these photons are attenuated before they emerge from the inspected object. Therefore, under the single-scatter approximation, the amount of energy scattered by dV and received by d^2r per unit time is

$$h\nu\dot{\Phi}_{\rm pri}(r',z)\mathfrak{n}_{\rm a}(r',z)\frac{z}{R^3} \times\left(\alpha_\nu(\ell)\frac{d\sigma^{\rm R}(\theta)}{d\Omega}+\alpha_{\nu_\theta}(\ell)\frac{\nu_\theta}{\nu}\frac{d\sigma^{\rm C}(\theta)}{d\Omega}\right)d^2r'dzd^2r \qquad (16)$$

where $\ell = [(r',z)(r,0)]$ and where ν_θ denotes the frequency of Compton photons deflected through angle θ, that is, $\nu_\theta = \nu/(1+\kappa(1-\cos\theta))$ with $\kappa = h\nu/m_{\rm e}c^2$ ($m_{\rm e}$ is the electron rest-mass and c is the velocity of light). Then, if we assume a distant point source, integrating (16) over r' and z gives the total amount of scattered energy received by d^2r per unit time, that is, $\mathcal{I}_{\rm scat}(r)d^2r$. It comes up that $\mathcal{I}_{\rm scat}$ can be connected to the primary irradiance $\mathcal{I}_{\rm pri}$ via an inhomogeneous Fredholm equation of the first kind:

$$\mathcal{I}_{\rm scat}(r) = \int_{\Pi_{\rm d}}\mathcal{I}_{\rm pri}(r')\mathcal{K}(r,r')d^2r' \qquad (17)$$

where $\mathcal{I}_{\rm pri}(r) = h\nu\dot{\Phi}_0(r)\alpha_\nu([(r,z^\star)(r,0)])$ and where the kernel $\mathcal{K}$ is given by

$$\mathcal{K}(r,r') = \int_0^{z^\star}\frac{z\mathfrak{n}_{\rm a}(r',z)}{R^3\alpha_\nu\left([(r',z)(r',0)]\right)} \times\left(\alpha_\nu(\ell)\frac{d\sigma^{\rm R}(\theta)}{d\Omega}+\alpha_{\nu_\theta}(\ell)\frac{\nu_\theta}{\nu}\frac{d\sigma^{\rm C}(\theta)}{d\Omega}\right)dz. \qquad (18)$$

Let us apply this result to the arrangement shown in Fig. 6(a), which is closely representative of the acquisition geometry described in Section II. The inspected iron specimen, with uniform thickness of 7 cm, includes a spherical defect of radius 5 mm (the spherical shape assumption simplifies computations). Clearly, if the distance from r' to r_0 is large enough (e.g., of the order of the sample thickness), then $\mathcal{K}(r,r') \approx \widetilde{\mathcal{K}}(r-r')$ for all r, where $\widetilde{\mathcal{K}}$ denotes the shift-invariant point spread function ob-

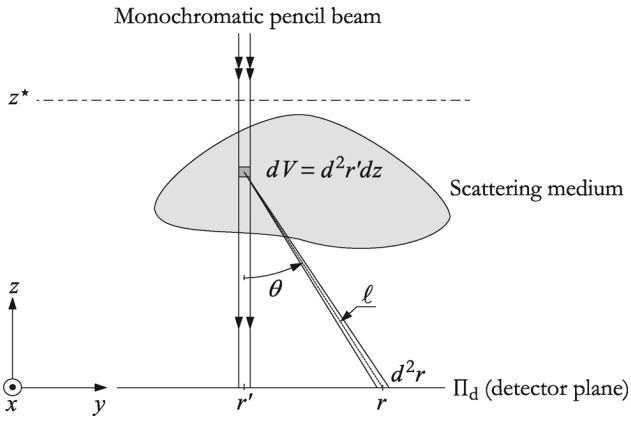

Fig. 5. Simple transmission imaging arrangement in which a scattering medium (the inspected object) is irradiated by a thin pencil of rays.

tained from (18) in the case of a flawless specimen. In fact, the most marked difference between $\mathcal{K}$ and $\widetilde{\mathcal{K}}$ is observed for $r' = r_0$. These kernels are displayed in Fig. 6(b) for the two extreme spectrum lines of iridium-192 with transition probability greater than 0.05% (i.e., $h\nu = 0.201$ MeV and $h\nu = 1.062$ MeV). In both cases, $\mathcal{K}(r,r_0)$ and $\widetilde{\mathcal{K}}(r-r_0)$ are close enough to conclude that $\mathcal{K}(r,r') \approx \widetilde{\mathcal{K}}(r-r')$ is a suitable approximation for all r and for all r'. It follows that (17) is well described by a convolution whose modulation transfer function is depicted in Fig. 6(c) for $h\nu = 0.201$ MeV and $h\nu = 1.062$ MeV. The corresponding -20 dB cut-off frequencies (about 0.11 mm^{-1} and 0.06 mm^{-1}) indicate that the unscattered defect signal is attenuated by a factor of at least 10 if one of its local dimensions is smaller than 9 mm, which is the case in practice.

The preceding observations show that, under the single-scatter approximation, for any spectrum line of iridium-192, the flaw information to be found in the scattered component is substantially smoothed out and may therefore be neglected. Since the real (i.e., multiple-scatter) point spread function is broader than $\widetilde{\mathcal{K}}$, there is reasonable evidence that $\mathcal{I}_{\rm scat} \approx \widetilde{\mathcal{I}}_{\rm scat}$, where $\widetilde{\mathcal{I}}_{\rm scat}$ denotes the scattered irradiance in the absence of defect. To substantiate this approximation, we simulated the exposure producing the radiograph in Fig. 2(a) by Monte Carlo calculation. Without going into details, we considered a 230 $\times$ 230 detector array in contact with a 2 mm lead filter and we computed the trajectories of 10^9 photons. The resulting primary and scattered components are shown in Fig. 7(a) and Fig. 7(b), respectively, while Fig. 7(c) compares the associated row-means over the regions delimited by the dashed lines. The magnitude of the little bump in the scatter profile is ten times smaller than the magnitude of the primary flaw signal. Using this ratio, we can estimate the value of the peak signal-to-noise ratio (PSNR) of the scattered flaw signal in the real radiograph, which is about 3.5 dB (PSNR $= 20\log_{10}(\Delta_{\rm p}/\sigma)$, where $\Delta_{\rm p}$ is the peak-to-peak value of the considered signal and σ is the standard deviation of the noise). This example suggests that, as a first approximation, the field

$$\widetilde{B} := 1 + \mathcal{I}_{\rm scat}/\widetilde{\mathcal{I}}_{\rm pri}$$

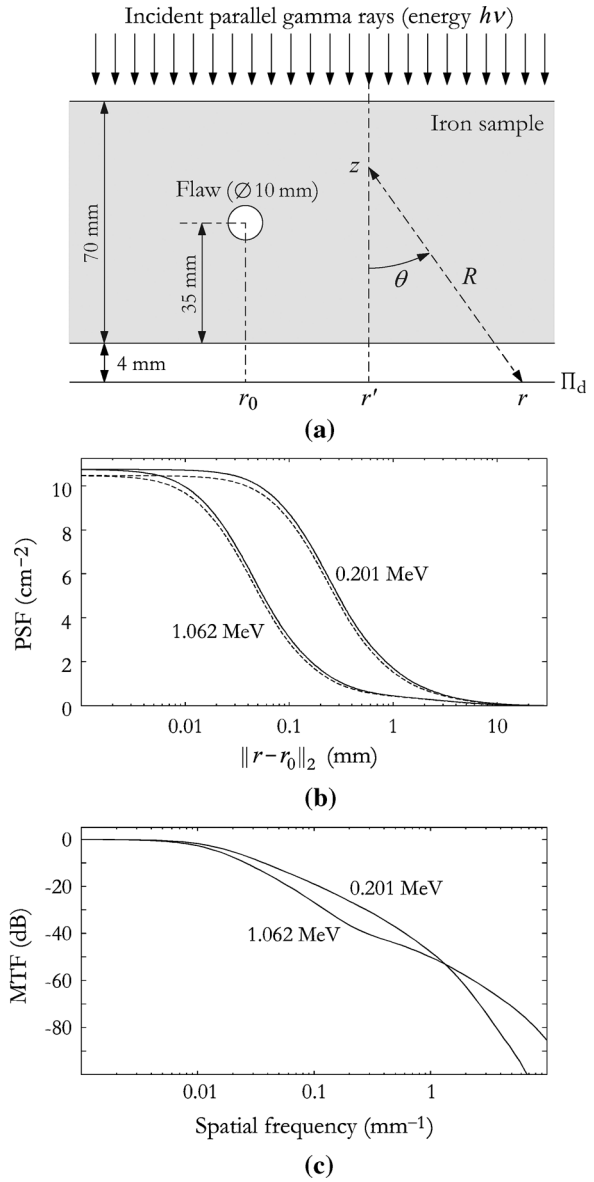

Fig. 6. Single-scatter approximation: (a) schematic of transmission imaging geometry; (b) point spread functions $\mathcal{K}(r, r_0)$ from (18) (dashed lines) and their shift-invariant approximations $\widetilde{\mathcal{K}}(r - r_0)$ (solid lines) for $h\nu = 0.201$ MeV and $h\nu = 1.062$ MeV; (c) modulation transfer functions of the shift-invariant approximations in (b).

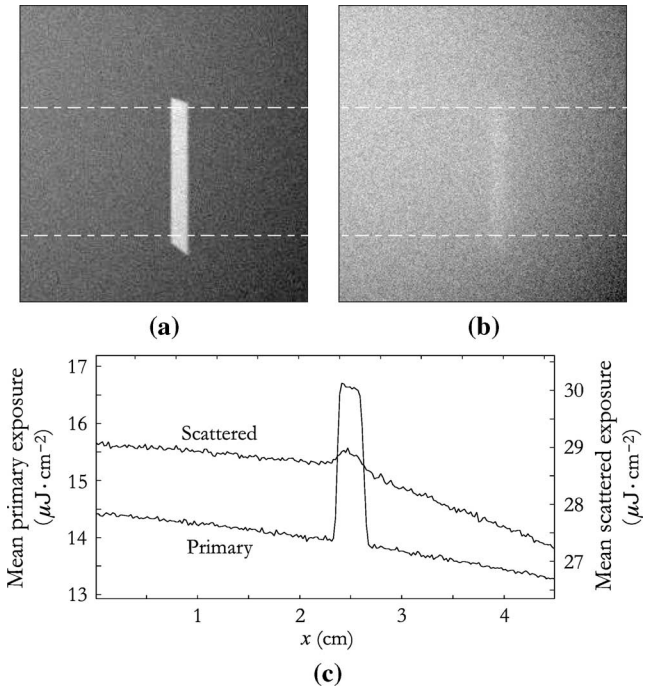

Fig. 7. Monte Carlo simulation of the radiograph shown in Fig. 2(a): (a) primary exposure $\tau\mathcal{I}_{\rm pri}$; (b) scattered exposure $\tau\mathcal{I}_{\rm scat}$; (c) means of the rows located between the dashed lines.

in (7) can be replaced by $1 + \widetilde{\mathcal{I}}_{\rm scat}/\widetilde{\mathcal{I}}_{\rm pri}$, that is, by the spatial distribution of the build-up factor corresponding to the flawless specimen. This approximation is more accurate in real situations, since the real defects of interest produce signals with lower SNR. However, should it be questionable whether the scattered flaw signal can be ignored, we take advantage of the fact that $\widetilde{B}$ is substantially smoother than Υ.

V. From Raw Radiographs to Line-Integral Projections

Let us review the present situation. From (7), and considering the conclusion of Section IV, we have

$$E[m,n] \approx \zeta_0 \widetilde{\Theta}_0[m,n] \left(\widetilde{B}[m,n] + \Upsilon[m,n] \right)$$

where $\zeta_0 := \tau\alpha_0 \mathcal{A} h\nu_0$ is the amount of energy released by the equivalent monochromatic source during exposure, $\widetilde{\Theta}_0$ is given by (9), and the notation $X[m,n]$ ($X = E$, $\widetilde{\Theta}_0$, $\widetilde{B}$ or Υ) stands for $\Delta^{-2} \int_{A_{m,n}} X(r) d^2 r$. Hence, from (11) and (14), the common logarithm of a digitized radiograph can be described by

$$\log_{10}(P(m,n)) \approx F_0(m,n) - \Gamma\zeta_0 \widetilde{\Theta}_0[m,n]\Upsilon[m,n] + \eta_1(m,n) \tag{19}$$

where F_0 is a smooth distribution representing the drift introduced by $\widetilde{\Theta}_0\widetilde{B}$ and by the digitization system, and where $\eta_1 \sim \mathcal{N}(0, \gamma^2\zeta_0\widetilde{\Theta}_0(\widetilde{B} + \Upsilon))$. In this model, F_0 and Υ are unknown fields, $\widetilde{\Theta}_0$ and $\widetilde{B}$ can be estimated based on the knowledge of the specimen geometry, and Γ, ζ_0 and γ are unknown scalars.

This section is devoted to the elaboration of processing techniques leading to a set $\{d^k; k = 1, \ldots, K\}$ of reduced size projections of the form

$$d^k(m,n) \approx \omega\Upsilon^k[m,n] + \eta^k(m,n) \tag{20}$$

where ω is a constant close to one and independent of k, and where η^k is some noise component to be characterized. We first show in Section V-A that the original data (19) can be subsampled without loss of flaw information. Then, in Section V-B, we propose a novel field-flattening algorithm which allows us to obtain projections of the form (20), but with ω depending on k. The removal of this residual dependency is discussed in Section V-C.

A. Subsampling

The useful bandwidth of the flaw signal is very limited because of geometric blurring as well as the presence of noise. We

can therefore reasonably assume that the available digital radiographs can be subsampled without risk. But how far can we go? Up to a multiplicative constant, dividing (19) by $\widetilde{\Theta}_0$ leads to the superposition of a very low frequency drift with the flaw information component Υ corrupted by some noise $\eta' \sim \mathcal{N}(0, \sigma'^2)$. Reasoning in the continuous domain and temporarily assuming that σ' is constant, the Fourier domain signal-to-noise ratio $\mathfrak{R}$ can be defined by $\mathfrak{R}(\xi) = \mathcal{S}_\Upsilon(\xi)/\mathcal{S}_{\eta'}(\xi)$, where $\xi := (u, v) \in \mathbb{R}^2$ and where $\mathcal{S}_\Upsilon$ and $\mathcal{S}_{\eta'}$ denote the power spectral densities of Υ and η', respectively. Since Υ is a transient signal, we have $\mathcal{S}_\Upsilon(\xi) = \mathrm{A}_\Upsilon^{-1}|\mathcal{F}_\Upsilon(\xi)|^2$, where A_Υ is the area of the support of Υ and $\mathcal{F}_\Upsilon$ stands for the 2-D Fourier transform of Υ. Besides, because the noise cut-off frequency is located beyond the bandwidth of Υ, we can model η' by a band-limited white noise with density $\mathcal{S}_{\eta'}(\xi) = (\sigma'\Delta)^2 \mathrm{rect}(\Delta u, \Delta v)$, where $\mathrm{rect}(x, y) = 1$ if $x, y \in]-1/2, 1/2[$, 0 otherwise. Hence, setting $\sigma_{\min} = \min\{\sigma'(m, n)\}$, we obtain

$$\mathfrak{R}(\xi) \leqslant \left(\mathrm{A}_\Upsilon \Delta^2 \sigma_{\min}^2\right)^{-1} |\mathcal{F}_\Upsilon(\xi)|^2$$

for all ξ in the Nyquist domain.

The information located in the frequency domain $\{\xi \in \mathbb{R}^2 \mid \mathfrak{R}(\xi) < 1\}$ is of no use for 3-D reconstruction. Consequently, if there exists a positive integer J such that

$$\forall \xi \in \mathbb{R}^2 \setminus \left[-1/(2^{J+1}\Delta), 1/(2^{J+1}\Delta)\right]^2, \quad |\mathcal{F}_\Upsilon(\xi)| < \mathrm{A}_\Upsilon^{1/2} \Delta \sigma_{\min} \qquad (21)$$

then the corresponding digitized radiograph can be subsampled by a factor of 2^J. In order to safely estimate J, we consider the very unfavorable (artificial) situation where the gamma-ray source and the defect are cuboids with edges parallel to the axes of a rectangular coordinate system whose (x, y)-plane coincides with the detector plane. Let A_S be the area of the (x, y)-base of the source and let θ_c be the maximum angle of incidence (25 degrees in our case). Under approximation (8), it can be shown [2] that

$$|\mathcal{F}_\Upsilon(\xi)| < \mu_0(\nu_0) \mathbb{I}_z (\pi^4 u^2 v^2 \mathrm{A}_S \cos\theta_c)^{-1}$$

with

$$\mathbb{I}_z := (z_2 - z_1)(1 + \mathcal{Q}^2/z_1 z_2) - 2\mathcal{Q}\ln(z_2/z_1)$$

where z_1 and z_2 respectively denote the minimum and maximum z-coordinates of the defect and $\mathcal{Q}$ is the distance from the source to the detector plane. It follows that

$$J \leqslant \frac{1}{4}\log_2\left(\frac{\pi^4 \mathrm{A}_S \cos\theta_c A_\Upsilon^{1/2} \sigma_{\min}}{\mu_0(\nu_0)\mathbb{I}_z \Delta^3}\right) - 1 =: J_{\sup} \qquad (22)$$

is a sufficient condition for (21) to hold. Note that, as we might expect, the upper bound $J_{\sup}$ is an increasing function of the source dimensions, the sampling rate and the noise standard deviation. As an example, $J_{\sup}$ is depicted in Fig. 8 as a function of A_Υ and $\sigma_{\min}$ for the testing conditions associated with radiographs (a)–(d) in Fig. 2. The corresponding pairs of values for A_Υ and $\sigma_{\min}$ are located between the level curves $J_{\sup}(\mathrm{A}_\Upsilon, \sigma_{\min}) = 2$ and $J_{\sup}(\mathrm{A}_\Upsilon, \sigma_{\min}) = 3$, which shows that subsampling by a factor of 4 does not affect the flaw information content (similar observations were made for radiographs (e)–(h) in Fig. 2). In practice, subsampling is achieved by keeping the low resolution residual stemming from subband decomposition of the original data (we use Johnston's filters [11]). This operation leaves description (19) unchanged, except for the noise standard deviation which must be divided by the subsampling factor.

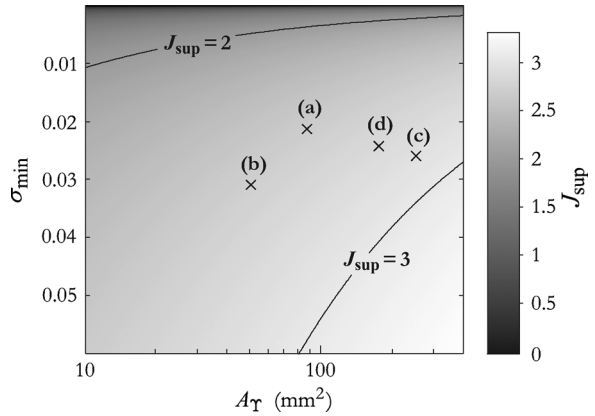

Fig. 8. Upper bound $J_{\sup}$ (22) for the logarithm to base 2 of the subsampling factor as a function of the area of the support of Υ and of the minimum noise standard deviation. The "×" marks correspond to radiographs (a)–(d) in Fig. 2.

B. Field-Flattening

Our goal here is to get rid of the smooth field F_0 in (19) so as to give access to Υ. We start from the data obtained by dividing $\log_{10} P$ by $\widetilde{\Theta}_0^{1/2}$, that is, projections of the form

$$P_{(1)} := \widetilde{\Theta}_0^{-1/2} \log_{10} P \approx \varphi - \Upsilon' + \eta' \qquad (23)$$

where $\varphi := \widetilde{\Theta}_0^{-1/2} F_0$, $\Upsilon' := \Gamma\zeta_0 \widetilde{\Theta}_0^{1/2} \Upsilon$, and $\eta' \sim \mathcal{N}(0, \sigma'^2)$ with $\sigma'^2 = 4^{-J}\gamma^2\zeta_0(\widetilde{B} + \Upsilon)$ (the factor of 4^{-J} is due to subsampling). Since metal thickness does not vary significantly over the projection region of interest, $\widetilde{B}$ is nearly constant outside the support Σ_Υ of Υ and its immediate neighborhood $\mathcal{N}_\Upsilon$ (for instance for the simulation results depicted in Fig. 7, $\widetilde{B}(r) \in [2.99, 3.07]$ if $r \notin \Sigma_\Upsilon \cup \mathcal{N}_\Upsilon$). Consequently, σ' approximately reduces to a constant, say ς, outside $\Sigma_\Upsilon \cup \mathcal{N}_\Upsilon$, whereas $\sigma' > \varsigma$ within Σ_Υ. With this in mind, the field-flattening operation is to produce an estimate $\widehat{\varphi}$ for φ in order to obtain projections proportional to Υ according to

$$P_{(2)} := \widetilde{\Theta}_0^{-1/2}\left(\widehat{\varphi} - P_{(1)}\right) \approx \Gamma\zeta_0\Upsilon + \eta_2 \qquad (24)$$

where $\eta_2 \sim \mathcal{N}(0, 4^{-J}\gamma^2\zeta_0\widetilde{\Theta}_0^{-1}(\widetilde{B} + \Upsilon))$. This is a non-trivial estimation task, not only because the spectra of the unknown fields φ and Υ' significantly overlap, but also because Σ_Υ cannot be assumed to be known in the prospect of automatic processing. In particular, spatial low-pass filtering is ineffective and standard polynomial fitting techniques produce biased estimations. Alternatively, a sophisticated method that apparently yields good results has been proposed in [12] and [13], but the resulting algorithm is cumbersome and has many parameters, some of which are difficult to set. For these reasons, we propose a new field-flattening approach that jointly estimates φ and ς

together with a continuous-valued representation of Σ_Υ. The corresponding algorithm is fairly simple to implement and involves few parameters that can be set without difficulty.

Let $\mathcal{G} = \{(x_m, y_n)\}$ be the regular grid supporting $P_{(1)}$. Since φ is the sampled version of a smooth surface, we identify it with the bicubic spline interpolant of a reduced size representation $\varphi_\downarrow$ defined on a coarse grid $\mathcal{G}_\downarrow = \{(x_i, y_j)\} \subset \mathcal{G}$ with node spacing $\Delta_\downarrow$; we shall use the notation $\varphi = \mathcal{S}_3\{\varphi_\downarrow\}$ for short. Assume for the moment that Σ_Υ is known and let χ be the field defined by

$$\chi(x_m, y_n) = \begin{cases} \rho & \text{if } (x_m, y_n) \notin \Sigma_\Upsilon \cup \mathcal{N}_\Upsilon \\ 0 & \text{otherwise} \end{cases}$$

where the constant ρ assures that $\sum_{\mathcal{G}} \chi(x_m, y_n) = |\mathcal{G}|$. Let us put

$$\chi_{i,j} := (\chi \circledast \mathcal{G})(x_i, y_j) \quad \text{and} \quad d_{i,j} := \left(P_{(1)} \circledast \mathcal{G}\right)(x_i, y_j)$$

where $\circledast$ stands for the 2-D discrete convolution operator over $\mathcal{G}$ and where $\mathcal{G}$ is a Gaussian function with standard deviation $\Delta_\downarrow/2$ satisfying $\sum_{\mathcal{G}} \mathcal{G}(x_m, y_n) = 1$. Then, φ can be approximated by $\widehat{\varphi} = \mathcal{S}_3\{\varphi_\downarrow(\chi)\}$ with

$$\varphi_\downarrow(\chi) := \arg\min_v \left\{ \sum_{i,j} \chi_{i,j}(v_{i,j} - d_{i,j})^2 + \lambda U_2(v) \right\} \quad (25)$$

where the regularization term U_2 is the discrete version of the thin plate spline functional (see, e.g., [14], [15]) and the free parameter $\lambda \geqslant 0$ adjusts the degree of stabilization of the solution. In practice, this minimization task can be solved efficiently by means of fast surface approximation algorithms such as the ones described in [16], [17] or [18]. We also have $\varsigma \approx \varsigma(\chi, \widehat{\varphi})$ with

$$\varsigma(\chi, \varphi) := \left(|\mathcal{G}|^{-1} \sum_{\mathcal{G}} \left[\chi \left(\varphi - P_{(1)} \right)^2 \right] (x_m, y_n) \right)^{1/2}. \quad (26)$$

In the case where Σ_Υ is unknown, these observations suggest to design an iterative algorithm that jointly evaluates φ and ς through alternate updating of the associated estimates together with a hidden field representing the accumulated knowledge about Σ_Υ. Let us respectively denote the estimates for φ, ς and χ at step q by φ_q, ς_q and χ_q. Appealing to definitions (25) and (26), and given $\varepsilon \in]0, 1[$, the proposed algorithm is of the following form:

$$\begin{array}{l} \chi_0 \leftarrow \text{constant field with value 1} \\ \varphi_0 \leftarrow \mathcal{S}_3\{\varphi_\downarrow(\chi_0)\} \\ \varsigma_0 \leftarrow \varsigma(\chi_0) \\ \textbf{repeat } \chi_{q+1} \leftarrow \rho_{q+1}\Xi(\chi_q; \varphi_q, \varsigma_q) \\ \qquad \varphi_{q+1} \leftarrow \mathcal{S}_3\{\varphi_\downarrow(\chi_{q+1})\} \\ \qquad \varsigma_{q+1} \leftarrow \varsigma(\chi_{q+1}, \varphi_{q+1}) \\ \textbf{until } |\varsigma_q - \varsigma_{q+1}| \leqslant \varepsilon\varsigma_0 \end{array} \quad (27)$$

The role of the constant ρ_{q+1} is to guarantee that $\sum_{\mathcal{G}} \chi_{q+1}(x_m, y_n) = |\mathcal{G}|$ and the updating mechanism Ξ is designed to relax the hidden field χ_q at locations that are likely to be within $\Sigma_\Upsilon \cup \mathcal{N}_\Upsilon$. The precise specification of Ξ relies on the definition of the local noise standard deviation estimate

$$\sigma_q := \left(\left(\varphi_q - P_{(1)}\right)^2 \circledast \mathcal{G} \right)^{1/2}$$

together with an additional parameter $\beta \in]0, 1[$ that expresses the noise standard deviation tolerance outside $\Sigma_\Upsilon \cup \mathcal{N}_\Upsilon$. Denoting the total number of iterations of the algorithm by Q, we wish to have $\sigma_Q(x_m, y_n) \leqslant (1 + \beta)\varsigma$ for all $(x_m, y_n) \notin \Sigma_\Upsilon \cup \mathcal{N}_\Upsilon$. To see how this can be achieved, note that we always have either $\varsigma_q > \varsigma$ or $\varsigma_q \approx \varsigma$ because of the bias produced by the flaw signal together with the fact that φ_q is a very smooth discrete surface. Hence, $\sigma_q(x_m, y_n) > (1 + \beta)\varsigma_q$ means that (x_m, y_n) is likely to be in $\Sigma_\Upsilon \cup \mathcal{N}_\Upsilon$ so that χ_q should be relaxed at this location. Moreover, in such a situation, the greater the difference $\sigma_q(x_m, y_n) - (1+\beta)\varsigma_q$, the more $\chi_q(x_m, y_n)$ should be loosened. There are, of course, many ways to get this behavior. We suggest the following point-wise updating scheme:

$$\begin{aligned} &(\Xi(\chi_q; \varphi_q\varsigma_q))(x_m, y_n) \\ &\quad = \begin{cases} \chi_q(x_m, y_n) \frac{\overline{\sigma}_q - \sigma_q(x_m, y_n)}{\overline{\sigma}_q - (1+\beta)\varsigma_q} & \text{if } \sigma_q(x_m, y_n) > (1+\beta)\varsigma_q \\ \chi_q(x_m, y_n) & \text{otherwise} \end{cases} \end{aligned}$$

where $\overline{\sigma}_q := \max_{\mathcal{G}} \sigma_q(x_m, y_n)$.

The algorithm described above involves four parameters, namely the node spacing $\Delta_\downarrow$ of the coarse grid $\mathcal{G}_\downarrow$, the regularization parameter λ in (25), the positive real ε fixing the stop criterion, and the noise standard deviation tolerance β. The choice of these parameters does not pose any special problem under testing conditions similar to those described in Section II. For instance, a 20×20 grid $\mathcal{G}_\downarrow$ is sufficient to capture the variations of the drift φ. Also, because of prior smoothing by $\mathcal{G}$, the solutions we are looking for via (25) are very close to the $d_{i,j}$'s at those locations where $\chi_{i,j} \geqslant 1$; consequently, setting $\lambda = 1.0$ is enough for the resulting surfaces to fit the thin plate constraint tightly (note that λ can always be selected by means of generalized cross-validation [19] or by using the L-curve method [20] at the expense of a substantial increase in computational load). Finally, choosing $\varepsilon = 10^{-4}$ gives satisfactory precision and setting $\beta = 5 \cdot 10^{-2}$ permits one to cope with low contrast flaw information.

As a first example, let us consider the case of projection (d) in Fig. 2. In accordance with the results of Section V-A, the associated input projection $P_{(1)}$ (23) shown in Fig. 9(a) was computed after subsampling P by a factor of 4. Using the proposed set of parameter values, our algorithm took 90 iterations to produce the estimates for χ and φ respectively depicted in Figs. 9(b) and (c). The absolute value of the resulting projection $P_{(2)}$ (24) is displayed in Fig. 9(d). A few insignificant irregularities caused by film manipulation are visible. Aside from these, the estimated hidden field provides a faithful representation of Σ_Υ that can be used for computing a 3-D region of interest for reconstruction. The second example depicted in Fig. 10 concerns projection (c) in Fig. 2; the results displayed in Figs. 10(b) and (c) were obtained in 63 iterations. Fig. 10(d) superimposes the intensity profiles of the input projection and the estimate for φ along the indicated dashed

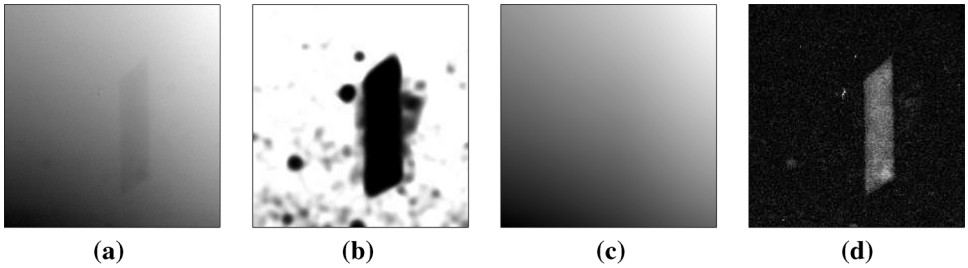

Fig. 9. Application of the field-flattening algorithm to projection (d) in Fig. 2: (a) associated input projection $P_{(1)}$ (23); (b) estimate for χ; (c) estimate for φ; (d) absolute value of the resulting projection $P_{(2)}$ (24).

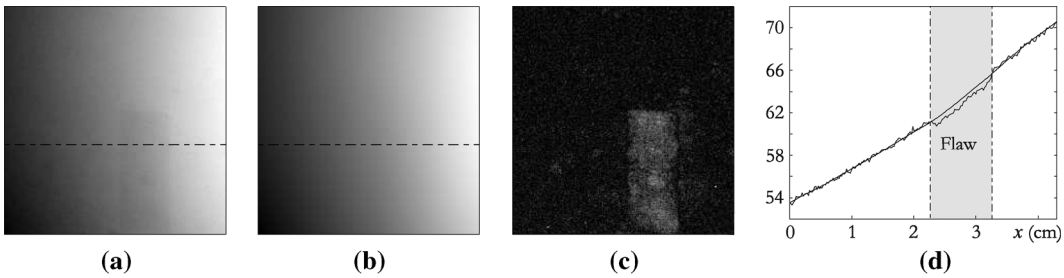

Fig. 10. Application of the field-flattening algorithm to projection (c) in Fig. 2: (a) associated input projection $P_{(1)}$ (23); (b) estimate for φ; (c) absolute value of the resulting projection $P_{(2)}$ (24); (d) intensity profiles of (a) and (b) along the dashed lines.

lines. It shows that the algorithm behaves well in very low constrast situations.

C. Calibration

The field-flattening process leads to a set $\{P^k_{(2)};\ k = 1,\dots,K\}$ of projections of the form

$$P^k_{(2)} \approx \Gamma\zeta^k_0\Upsilon^k + 2^{-J}\gamma\eta\left[\zeta^k_0(\widetilde{B}^k + \Upsilon^k)/\widetilde{\Theta}^k_0\right]^{1/2} \tag{28}$$

where $\eta \sim \mathcal{N}(0,1)$. While the film sensitivity measure Γ obviously does not depend on k, it is not so clear that γ is the same for each projection. In fact, γ is defined by the quantum efficiency of the detector and by the mean number of halide grains that are made developable per absorbed quantum. Strictly speaking, because of the latter dependency, γ is a function of both incidence angle and metal thickness and hence varies with k. However, within our framework, the angle of incidence and the specimen thickness latitude are limited enough to disregard the variations in γ between any two projections of a same set.

We want to remove the unknown factor $\Gamma\zeta^k_0$ in (28) up to some multiplicative constant independent of k and close to one. Recall that our field-flattening algorithm provides an estimate $\widehat{\varsigma}$ for the noise standard deviation in $P_{(1)}$ (23) outside Σ_Υ. More specifically, for each k, we have the value of

$$\widehat{\varsigma}^k \approx 2^{-J}\gamma\left(\zeta^k_0\overline{B}^k\right)^{1/2} \tag{29}$$

where $\overline{B}^k$ stands for the mean build-up factor over the support Σ^k of projection k. Since $\overline{B}^k$ can be estimated via Monte Carlo simulation in a reasonable amount of time, we choose to multiply each $P^k_{(2)}$ by $\overline{B}^k/(\widehat{\varsigma}^k)^2$, which leads to projection data of the form $4^J\Gamma\gamma^{-2}\Upsilon^k$ plus some noise. We are then left with the problem of estimating $\Gamma\gamma^{-2}$. Because we are not actually looking for a very sharp estimate, we can resort to mean behavior approximations. Let us drop the index k for a moment. According to (14), the standard deviation of $D(m,n)$ is approximately equal to $\gamma(E[m,n])^{1/2}$ and thus $\gamma \approx \overline{\sigma}^D_{\setminus\Upsilon}/(\overline{E}_{\setminus\Upsilon})^{1/2}$ where $\overline{\sigma}^D_{\setminus\Upsilon}$ and $\overline{E}_{\setminus\Upsilon}$ respectively stand for the mean standard deviation of the density and the mean exposure over $\Sigma \setminus \Sigma_\Upsilon$. Hence, from (10),

$$\gamma \approx \overline{\sigma}^D_{\setminus\Upsilon}\Gamma^{1/2}(\overline{D} - D_{\min})^{-1/2}$$

where $\overline{D}$ is the average film density fixed by testing specifications (about 2.5 in our case). Substituting into (29) gives

$$\widehat{\varsigma} \approx 2^{-J}\overline{\sigma}^D_{\setminus\Upsilon}\left[\frac{\Gamma\zeta_0\overline{B}}{\overline{D} - D_{\min}}\right]^{1/2}. \tag{30}$$

At the same time, relations (11) and (23) show that $\widehat{\varsigma}$ is also an estimate for the mean standard deviation of the fluctuations of $\widetilde{\Theta}_0^{-1/2}D$ outside Σ_Υ. Therefore

$$\widehat{\varsigma} \approx 2^{-J}\overline{\Theta}_0^{-1/2}\overline{\sigma}^D_{\setminus\Upsilon} \tag{31}$$

where $\overline{\Theta}_0 := \int_\Sigma \widetilde{\Theta}_0(r)d^2r / \int_\Sigma d^2r$. It follows from (30) and (31) that

$$\Gamma\zeta_0 \approx (\overline{D} - D_{\min})/\overline{\Theta}_0\overline{B}. \tag{32}$$

The value of $\sum_{k=1}^K \zeta^k_0$ can be estimated from either (29) or (32). Setting the corresponding expressions equal to each other, we obtain

$$4^J\Gamma\gamma^{-2} \approx \frac{(\overline{D} - D_{\min})\sum_{k=1}^K \frac{1}{\overline{\Theta}^k_0\overline{B}^k}}{\sum_{k=1}^K \frac{(\zeta^k)^2}{\overline{B}^k}} =: c_\gamma. \tag{33}$$

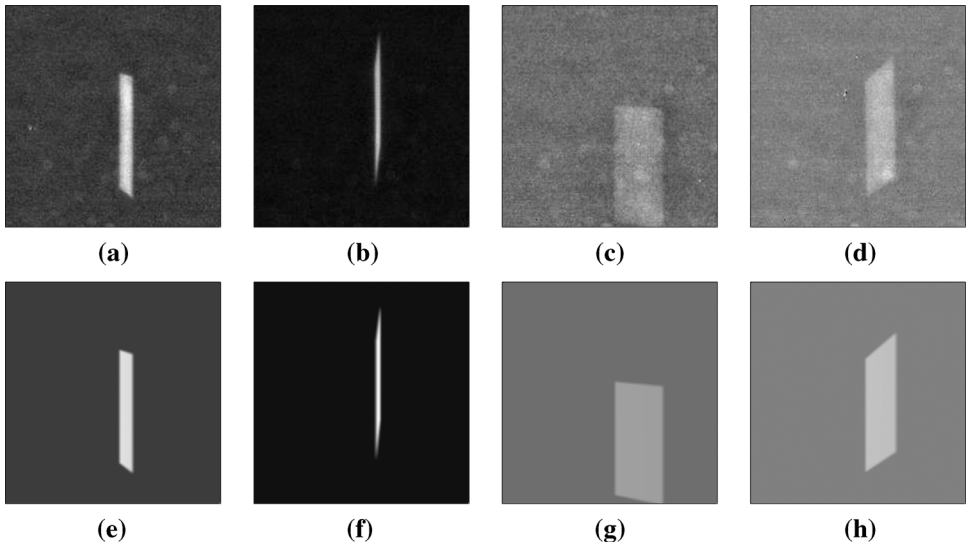

Fig. 11. Processing of projections (a)–(d) in Fig. 2: (a)–(d) final outputs; (e)–(h) representation of the corresponding simulated flaw signals using the same gray level mappings (the background intensity value is zero).

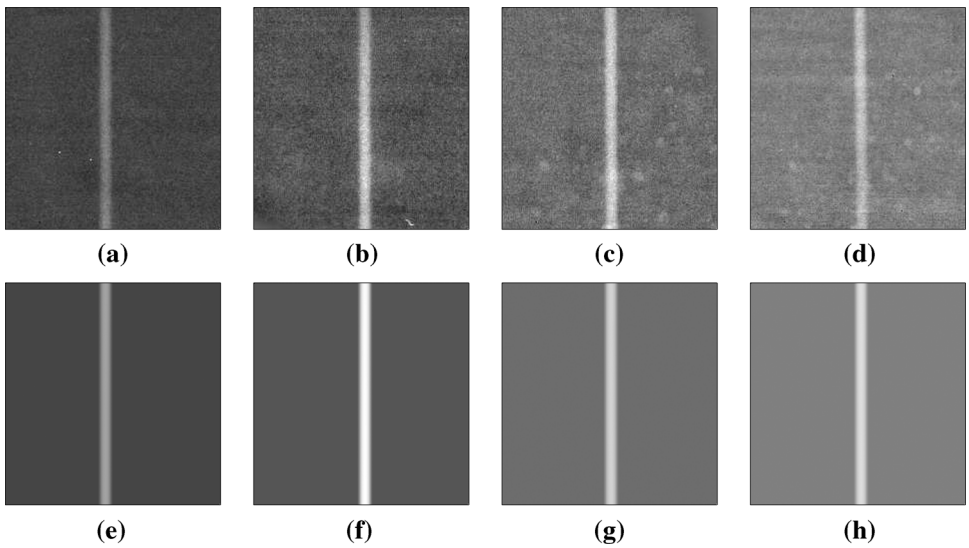

Fig. 12. Processing of projections (e)–(h) in Fig. 2: (a)–(d) final outputs; (e)–(h) representation of the corresponding simulated flaw signals using the same gray level mappings.

In the end, multiplying each $P^k_{(2)}$ (28) by $\overline{B}^k/c_\gamma(\widehat{\varsigma}^k)^2$ produces data of the required form, that is, a set $\{d^k; k = 1, \ldots, K\}$ of projections such that

$$d^k \approx \omega \Upsilon^k + \omega' \eta \left[(\widetilde{B}^k + \Upsilon^k)/\widetilde{\Theta}^k_0 \zeta^k_0 \right]^{1/2} \tag{34}$$

where ω is close to one and $\omega' \approx 2^{-J}\gamma\Gamma^{-1}$. To confirm this result, Figs. 11(a)–(d) and 12(a)–(d) show the outputs d^k of the full processing procedure for the raw data in Fig. 2. The corresponding simulations of $\Upsilon^k[m,n] = \Delta^{-2}\int_{A_{m,n}} \Upsilon^k(r)d^2r$ (see (8)) are respectively represented in Figs. 11(e)–(h) and 12(e)–(h) using the same gray level mappings for suitable comparison. Apart from noise, each processed projection is very close to its simulated counterpart, which gives strong credit to our image formation model as well as to the proposed processing techniques. Note that if the metal thickness exhibits moderate variations over the projection regions of interest, then so do $\widetilde{B}^k$ and $\widetilde{\Theta}^k_0$, and it follows that the noise component in (34) is approximately stationary outside Σ_{Υ^k}. Besides, although ω' is unknown, the mean noise variance outside Σ_{Υ^k} can be easily estimated by appealing to the description of Σ_{Υ^k} provided by the field-flattening algorithm.

VI. Summary and Conclusion

We have proposed a complete radiographic image formation model together with a detailed processing procedure to set the basis for 3-D reconstruction of defects in thick metal components. The raw data consists of a set $\{P^k; k = 1, \ldots, K\}$ of projections whose common logarithm has been shown to satisfy

$$\log_{10} P^k \approx F^k_0 - \Gamma\zeta^k_0\widetilde{\Theta}^k_0\Upsilon^k + \eta^k_1$$

where η^k_1 is Gaussian white noise with mean zero and variance $\gamma^2\zeta^k_0\widetilde{\Theta}^k_0(\widetilde{B}^k + \Upsilon^k)$ (we refer to the very beginning of Section V

for details). Starting from this model, extraction of the flaw information signals is completed in four stages.

1) *Subsampling*: replace each $\log_{10} P^k$ by the low resolution residual of its subband decomposition at level $J \leqslant J_{\sup}$ (see (22)).
2) Perform *preliminary computations* based on the knowledge of the specimen geometry: (i) compute the equivalent monochromatic source energies $h\nu_0^k$ defined in Section III-A; (ii) compute the fields $\widetilde{\Theta}_0^k$ according to (9); (iii) estimate the mean build-up factors $\overline{B}^k$ by Monte Carlo simulations.
3) *Field-Flattening*: estimate the fields $\varphi^k := F_0^k(\widetilde{\Theta}_0^k)^{-1/2}$ by applying algorithm (27) to each

$$P_{(1)}^k := \left(\widetilde{\Theta}_0^k\right)^{-1/2} \log_{10} P^k.$$

This gives projections of the form

$$P_{(2)}^k := \left(\widetilde{\Theta}_0^k\right)^{-1/2} \left(\widehat{\varphi}^k - P_{(1)}^k\right) \approx \Gamma \zeta_0^k \Upsilon^k + \eta_2^k$$

together with some estimates $\widehat{\varsigma}^k$ for the noise standard deviation in $P_{(1)}^k$ outside the support of Υ^k.
4) *Calibration*: Multiply each $P_{(2)}^k$ by $\overline{B}^k/c_\gamma(\widehat{\varsigma}^k)^2$, where c_γ is defined in (33), to obtain the final projection data $d^k \approx \omega \Upsilon^k + \eta^k$, where the constant ω is close to one and where η^k is a Gaussian white noise field whose variance is proportional to $(\widetilde{B}^k + \Upsilon^k)/\widetilde{\Theta}_0^k$.

Using approximation (8), the fully processed projections are of the form

$$d^k(m,n) \approx \frac{\omega \mu_0\left(\nu_0^k\right)}{\mathcal{V}\Delta^2} \int_{S^k} \int_{A_{m,n}^k} L_{\text{flaw}}(s,r) d^2 r d^3 s + \eta^k(m,n). \tag{35}$$

To see why these data are suitable for reconstruction, let us introduce a 3-D voxel lattice V and let $x^0 = \{x_v^0; v \in V\}$ be the $[0,\omega]$-valued distribution defined as follows: for all v, x_v^0 is linearly proportional to the volume of the intersection of v with the defects and $x_v^0 = \omega$ if v is entirely included in a defect. Then

$$L_{\text{flaw}}(s,r) \approx \omega^{-1} \sum_{v \in V} x_v^0 L_v(s,r)$$

where $L_v(s,r)$ is the length of the intersection between $[sr]$ and v. Besides, the integrals

$$\mathcal{I}_{m,n,v}^k := \frac{1}{\mathcal{V}\Delta^2} \int_{S^k} \int_{A_{m,n}^k} L_v(s,r) d^2 r d^3 s$$

can be estimated by Monte Carlo integration:

$$\mathcal{I}_{m,n,v}^k \approx \frac{1}{N_s N_r} \sum_{i,j} L_v(s_i, r_j) =: \rho_{m,n,v}^k$$

where $\{s_i; i = 1,\ldots,N_s\}$ and $\{r_j; j = 1,\ldots,N_r\}$ are some sets of points picked uniformly at random from S^k and $A_{m,n}^k$, respectively. It follows that

$$d^k(m,n) \approx \sum_{v \in V} x_v^0 \underbrace{\mu_0\left(\nu_0^k\right) \rho_{m,n,v}^k}_{=: h_{m,n,v}^k} + \eta^k(m,n)$$

that is

$$d^k \approx \mathcal{H}^{(k)}(x^0) + \eta^k$$

where the matrix representation of the linear map $\mathcal{H}^{(k)}$ from $\mathbb{R}^{|V|}$ to $\mathbb{R}^{|G^k|}$ has the $h_{m,n,v}^k$'s as entries.

Finally note that reconstruction from $\{d^k; k = 1,\ldots,K\}$ cannot be binary-valued as ω is not perfectly known. However, since the order of magnitude of ω is fixed, reconstruction can be carried out by considering a finite set of possible voxel values (e.g., an 8-bit volume). This issue is addressed in another paper [1] in which we propose a new stochastic approach whose results further validates the present work.

REFERENCES

[1] M. C. Robini, A. Lachal, and I. E. Magnin, "A stochastic continuation approach to piecewise constant reconstruction," *IEEE Trans. Image Process.*, to be published.

[2] M. C. Robini, "Bayesian Inversion of ill-posed problems using stochastic relaxation with annealing. Application to image restoration and 3-D reconstruction from a very limited number of projections," (in French) Ph.D. dissertation, INSA-Lyon Scientific and Tech. Univ., Lyon, France, Dec. 1998.

[3] R. Azencott, B. Chalmond, F. Coldefy, and B. Lavayssière, "Détection, reconstruction 3-D et caractérisation de défauts à partir d'images radiographiques," in *Proc. Int. Conf. Quality Control by Artificial Vision*, Le Creusot, France, May 1995, pp. 25–36.

[4] B. Chalmond, F. Coldefy, and B. Lavayssière, "Tomographic reconstruction from non-calibrated noisy projections in non-destructive evaluation," *Inverse Probl.*, vol. 15, pp. 399–411, 1999.

[5] A. Mohammad-Djafari and C. Soussen, "Reconstruction of compact homogeneous 3-D objects from their projections," in *Discrete Tomography: Foundations, Algorithms and Applications*, G. T. Herman and A. Kuba, Eds. Boston, MA: Birkhäuser, 1999, pp. 317–342.

[6] C. Soussen and A. Mohammad-Djafari, "Contour-based models for 3-D binary reconstruction in X-ray tomography," in *Proc. 20th Int. Workshop on Bayesian Inference and Maximum Entropy Methods in Sci. and Eng.*, Gif-sur-Yvette, France, Jul. 2000, pp. 1–12.

[7] R. H. Herz, *The Photographic Action of Ionizing Radiations in Dositometry and Medical, Industrial, Neutron, Auto- and Microradiography*. New York: Wiley, 1969.

[8] R. Halmshaw, *Industrial Radiology. Theory and Practice*. London, U.K.: Applied Science Publishers, 1982.

[9] L. E. Bryant and P. McIntire, Eds., *Radiography and Radiation Testing*, 2nd ed. Columbus, OH: American Society for Nondestructive Testing, 1985, vol. 3, Nondestructive testing handbook.

[10] J. H. Hubbell, "Photon cross sections, attenuation coefficients, and energy absorption coefficients from 10 keV to 100 GeV," *Nat. Stand. Ref. Data Ser., Nat. Bur. Stand.*, vol. 29, Aug. 1969.

[11] J. D. Johnston, "A filter family designed for use in quadrature mirror filter banks," in *Proc. IEEE Int. Conf. Acoust., Speech, Signal Process.*, Denver, CO, Apr. 1980, pp. 291–294.

[12] R. Azencott, B. Chalmond, and F. Coldefy, "Association of adaptative smoothing and Markovian models for detection of valley bottoms on strongly noisy images," in *Proc. 11th IAPR Int. Conf. Patt. Recognition*, La Hague, France, Aug. 1992, vol. 3, pp. 327–330.

[13] R. Azencott, B. Chalmond, and F. Coldefy, "Markov fusion of a pair of noisy images to detect intensity valleys," *Int. J. Comput. Vis.*, vol. 16, no. 2, pp. 135–145, 1995.

[14] D. Terzopoulos, "Computing Visible-Surface Representations," Artif. Intell. Lab., Mass. Inst.Technol., Cambridge, MA, A.I. Memo 800, 1985.

[15] D. Terzopoulos, "Regularization of inverse visual problems involving discontinuities," *IEEE Trans. Pattern Anal. Mach. Intell.*, vol. 8, no. 4, pp. 413–424, Apr. 1986.
[16] D. Terzopoulos, "Multilevel computational processes for visual surface reconstruction," *Comput. Vision Graph. Image Process.*, vol. 24, pp. 52–96, 1983.
[17] R. Szeliski, "Fast surface interpolation using hierarchical basis functions," *IEEE Trans. Pattern Anal. Mach. Intell.*, vol. 12, no. 6, pp. 513–528, Jun. 1990.
[18] M.-H. Yaou and W.-T. Chang, "Fast surface interpolation using multiresolution wavelet transform," *IEEE Trans. Pattern Anal. Mach. Intell.*, vol. 16, no. 7, pp. 673–688, Jul. 1994.
[19] G. H. Golub, M. Heath, and G. Wahba, "Generalized cross-validation as a method for choosing a good ridge parameter," *Technometrics*, vol. 21, no. 2, pp. 215–223, 1979.
[20] C. Hansen, "Analysis of discrete ill-posed problems by means of the L-curve," *SIAM Rev.*, vol. 34, no. 4, pp. 561–580, 1992.